# Effect of Crystallization of Cu$_2$ZnSnS$_x$Se$_{4−x}$ Counter Electrode on the Performance for Efficient Dye-Sensitized Solar Cells

Hongli Chen, Dongxing Kou,* Zhixian Chang, Wenhui Zhou, Zhengji Zhou, and Sixin Wu*

The Key Laboratory for Special Functional Materials of MOE, Henan University, Kaifeng, 475004, P. R. China

ABSTRACT: Cu$_2$ZnSnS$_x$Se$_{4−x}$ (CZTSSe) counter electrodes (CEs) in dye-sensitized solar cells (DSSCs) are commonly developed with porous structures, but their high surface area could also retard electron transport processes owing to the abundant grain boundaries. Herein, we employed a convenient solution method and a rapid heating process to prepare well crystalline CZTSSe CEs in DSSCs. The influence of crystallization of CZTSSe film on DSSCs performances was discussed in depth. The thermogravimetric analysis, phase morphology, conductivity, and electrochemical characteristics of CZTSSe films were performed. It is found that the rapid heating process is beneficial to the formation of well crystalline film with large grains. As the porosity and grain boundaries in the bulk film are dramatically reduced with the enhanced crystallization, the charge transport process is gradually improved. Using cyclic voltammogram and electrochemical impedance spectroscopy measurements, we propose that the accelerating charge transport is of great importance to the photovoltaic performances of DSSCs due to their superior electrocatalytic activities. As the highest cell efficiency was achieved, well crystalline CZTSSe is an efficient CE catalytic material.

KEYWORDS: Cu$_2$ZnSnS$_x$Se$_{4−x}$, crystallization, counter electrode, dye-sensitized solar cells
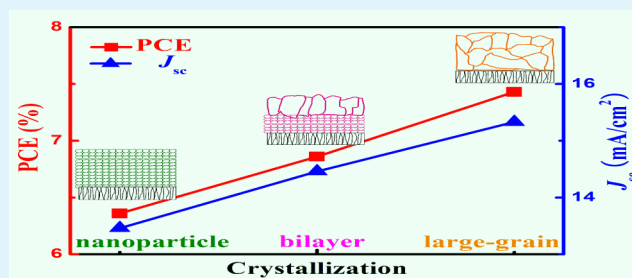
1. INTRODUCTION

Over the past years, dye-sensitized solar cells (DSSCs) are among the most promising photovoltaic devices for low-cost light-to-energy conversion with relatively high efficiency.[1−4] Up to now, a landmark cell efficiency over 13% has been obtained,[5] exhibiting a promising application foreground in renewable energy. The working mechanism of this device is based on the injection of electrons from excited states of dye to the conduction band of the semiconductor, followed by the reduction of the oxidized dye with a charge mediator.[6−10] During these processes, the counter electrode (CE) plays an important role in reducing triiodide to iodide. It has been known that Pt is a conventional CE material with good electrocatalytic properties, but its low abundance (0.0037 ppm) and the limited supply cannot meet the increasing demand for its broad applications. In addition, Pt is not effective as a CE for redox couples such as cobalt complexes, T$_2$/T$^−$, and polysulfide electrolytes used in solar cells.[11] Especially, the long-term working can lead to a dissolution and degradation of Pt CE.[12] Considerable attention has been drawn to exploring inexpensive substitutes, such as TiN, CoS, V$_2$O$_3$, Cu$_2$ZnSnS$_4$ (CZTS), and other copper chalcogenide-based compounds, and so forth.[13−15]

Narrow band gap p-type semiconductors as counter electrodes have opened a new way for the hybrid DSSCs technology. The earth-abundant multicomponent alloy Cu$_2$ZnSnS$_x$Se$_{4−x}$ (CZTSSe) is a more alternative material, due to its electronic structure and synergetic effects of the different components.[11] The facets of kesterite CZTSSe are of the alternate cation layer and anion layer, exhibiting charge imbalance and its polarity could be stabilized by absorbing the cations and/or the anions that could compensate the charge imbalance.[16] The surface atomic configuration should play a significant role on I$_3^−$ adsorption to induce better electrocatalytic properties. Though the exact reason for superior catalytic activity of the hybrids in DSSCs is not clear,[11] and the role of each part of the hybrid needs to be clarified in the future research, superior catalytic activities of the hybrids in DSSCs have been achived. Lee and co-workers[17] had shown a hierarchical nanoflake structured Cu$_2$ZnSnS$_4$ (CZTS) CE with high surface area via a facile solvothermal approach, which exhibited a higher cell efficiency than Pt. Zhan et al.[18] also reported a porous flower-like CZTS film as CE and proposed that this high surface area film increased conversion efficiency (7%) due to its efficient electrocatalytic activity. Yuan et al.[19] constructed rough CZTSe film with different thicknesses by decreasing the concentration of the precursor solution and found that an optimized thickness of the CZTSe layer was beneficial to the highest cell efficiency. Their findings generally suggest that the previous studies mainly focus on designing porous CZTS(Se) films with high surface area to improve the performance of DSSCs. However, though the large surface area contributes a higher electrocatalytic activity, it can also retard electron transport processes owing to the abundant

grain boundaries and defects, which impedes the further improvement of the DSSCs performances.[20]

In general, both high surface area for increasing activation sites and high conductivity for accelerating charge transport are important factors for an ideal CE with good electrocatalytic activity.[21,22] Herein, we employed a convenient solution method and a rapid heating process to prepare a well crystalline CZTSSe CE in DSSCs. We showed that the high-crystalline CZTSSe CE possessed superior conductivity and enhanced the efficiency of DSSCs, dramatically. Using cyclic voltammogram (CV) and electrochemical impedance spectroscopy (EIS) measurements, the influence of crystallization of CZTSSe film on DSSCs performances was discussed in depth. This provides a different approach to the design of CZTSSe CEs, which is generally not afforded by previous reports applying high surface area for better electrocatalytic properties, focuses on the improvement of crystallization for better charge transport, and holds for a more convenient way to optimize CE performances for efficient DSSCs.

2. EXPERIMENTAL SECTION

Materials. Copper(I) oxide, zinc(II) chloride dihydrate, and tin(IV) chloride pentahydrate were purchased from Alfa. Carbon disulfide (CS_2, 99.9%), 1-butylamine ($CH_3(CH_2)_3NH_2$, 99%), ethanol (CH_3CH_2OH, AR), selenium (Se, 99.9%) procured from Aladdin. All chemicals were used as received without any purification.

Preparation of CZTS Precursor Solution. First, 10.0 mL of ethanol, 3.6 mL of CS_2 (60.0 mmol), and 6.0 mL of 1-butylamine (60.0 mmol) were mixed in a 50 mL flask under magnetic stirring at room temperature. Afterward, Cu_2O (0.2146 g, ~1.5 mmol), zinc(II) chloride dihydrate (0.2044 g, ~1.5 mmol), and tin(IV) chloride pentahydrate (0.5259 g, ~1.5 mmol) were loaded into the flask with magnetic stirring at room temperature until all of the solid was dissolved and a orange-red solution was obtained. All of the procedures were conducted in the air.

Preparation of Precursor Films. The FTO glass substrates used in this study have a 1.5×2 cm^2 size area (Alfa). The CZTS precursor solution was spin-coated on the cleaned FTO glass substrate at 600 rpm for 9 s, then 2500 rpm for 20 s. Subsequently, a sintering process was employed in a 300 °C preheated furnace for 3 min in the air to form the CZTS precursor thin film with a monolayer thickness of ~280 nm. The CZTS precursor film with a final thickness of ~1.1 μm was acquired by repeating four spin-coating/air-sintering cycles.

Preparation of Different Crystalline CZTSSe Films. A postselenization process was utilized to recrystallize the precursor film into CZTSSe film. Selenium vapor was generated by the evaporation of 40 mg of Se powder mixed with Ar in a graphite box at 550 °C for 30 min. Evidently, different heating rates were employed during the selenization treatment for the purpose of acquiring CZTSSe films with different crystalline structures. A heating rate of 5 °C/min was employed to form small-sized nanoparticle structure film. With an increased heating rate up to 50 °C/min, a bilayer structure film with a large-grain layer on the top and a nanoparticle layer on the bottom was obtained. Finally, the large-grain structure film was acquired by pushing the precursor film into a preheated zone utilizing a push–pull rod, and it is typically with a heating rate of 150 °C/min.

BET Measurement. The surface area, pore volume, and pore size were evaluated by using a Micromeritics (TriStar II 3020 V1.03, Micromeritics Instrument Corporation) nitrogen adsorption/desorption apparatus. CZTSSe films on FTO were applied because the common measurement of powder samples cannot present the true morphology of the crystal films. The unit of surface area is also calculated in m^2/m^2, not m^2/g, to eliminate the effect of FTO. The area and weight of CZTSSe films with increasing heating rate are about 31.24, 34.54, and 32.46 mm^2 and 0.0778, 0.0896, and 0.0852 g, respectively.

DSSC Fabrication. The colloidal TiO_2 nanoparticles were prepared by hydrolysis of titanium tetraisopropoxide as described elsewhere.[23] Then, the obtained nanoparticles were mixed with polyethylene glycol to form the viscous paste. The colloidal paste was coated on a transparent conductive oxide (TCO) glass substrate by screen-printing. The films (0.25 cm^2) were dried at room temperature and then sintered at 510 °C for 30 min in the air. The photoelectrodes were immersed in a dye solution containing N719 at room temperature for 12 h. The platinized counter electrodes were obtained by spraying H_2PtCl_6 solution on TCO glass, followed by heating at 410 °C for 20 min. Then, the obtained Pt and CZTSSe counter electrodes were placed directly on top of the dyed TiO_2 films sealed with a 60 μm thermal adhesive film (Surlyn, Dupont). The electrolyte (0.1 M LiI, 0.1 M I_2, 1.0 M DMPII, and 0.5 M *tert*-butylpyridine in a liquid of acetonitrile) was filled from a hole on the counter electrode and then sealed with a Surlyn adhesive film under a cover glass by heating.

Sample Characterization. Thermogravimetric analysis (TGA) was conducted under a nitrogen flow (300 cm^3/min) at a heating rate of 3 °C/min using a TG/DTA 6200 thermogravimetric analyzer, SII, Inc. The crystal structure of the CZTSSe films was determined by X-ray diffraction (XRD, Philips X′ PertPro, Cu−Kα1: λ = 1.5406 Å) and Raman spectrum (LABRAM-1B confocal laser, λ = 632.8 nm). Cross-sectional images of the samples were taken using a field emission scanning electron microscope (SEM, JSM-5600LV at 20 kV). CV was carried out in a three-electrode system in an acetonitrile solution of 0.1 M LiClO$_4$, 10 mM LiI, and 1 mM I_2 at a scan rate of 50 mV s^{-1}. The Ag/Ag$^+$ couple served as a reference electrode, and platinum was used as a counter electrode. EIS was performed by an impedance measurement unit (ZAHNER-elektrik IM6) in the frequency range of $0.1-10^5$ Hz with an amplitude of 10 mV. The four-probe method on a digital source meter (Keithley 2400) was used to test the resistivity of the samples of different crystallization. The photo-current–voltage ($J-V$) measurements were produced by a solar simulator (Newport, Orielclass A, SP91160A, USA) under AM 1.5, 100 mW/cm^2 irradiation.

3. RESULTS AND DISCUSSION

The preheating process is necessary to remove the organic solvents in order to form a dense precursor film after each spin-coating. Figure 1 presents thermogravimetric analysis (TGA)
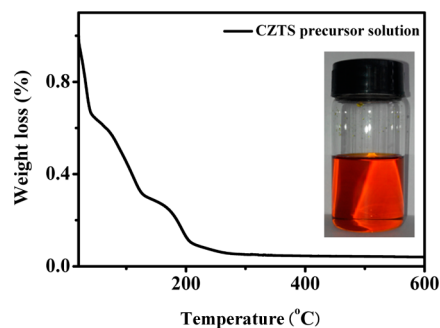

Figure 1. TG curve of the CZTS precursor. Inset: digital photograph of the CZTS precursor dissolved in ethanol.

data for the mixed CZTS precursor solution (Cu/(Zn + Sn) = 1, Zn/Sn = 1). The TGA sample was the same solution used in the experiment without any further treatment. It was found that the CZTS precursor exhibited a relatively fast weight loss from the room temperature to 125 °C, which contributed to the evaporation of low-boiling-point molecules (1-butylamine, CS_2, and ethanol). Another obvious weight loss occurred between 125 and 300 °C due to the precursor decomposition. According to the TGA data, the CZTS precursor is almost completely decomposed at 300 °C.[24−26]

High-temperature thermal annealing processes are nearly always employed for the as-fabricated nanocrystal films, and remarkable grain growth is required to improve carrier transport in the film and scattering from the boundaries between nanocrystals.[28] After preannealed CZTS precursor films were constructed on FTO glass, a postselenization process with a distinct heating rate followed. The representative cross-sectional view and surface topography SEM images of the selenized CZTSSe films are displayed in Figure 2. It can be seen
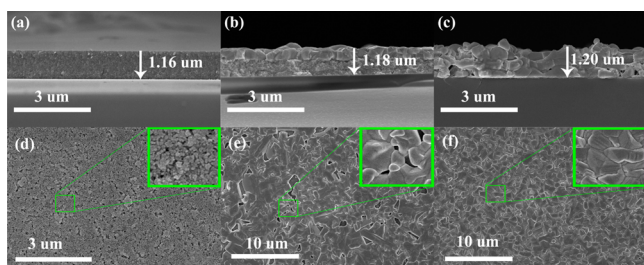

Figure 2. Cross-sectional view (a−c) and surface topography (d−f) SEM images of different crystalline CZTSSe films: (a, d) small-sized nanoparticle, (b, e) bilayer structure with a bottom small-sized nanoparticle layer and a top large-grain layer, and (c, f) large-grain.

that a nanoparticle film (5 °C/min), a bilayer film (50 °C/min), and a large-grain film (150 °C/min) are obtained, suggesting that the crystallization of CZTSSe film is gradually enhanced with the heating rate increased. Guo et al.[27] proposed that the formation of large grains is enabled by a lattice expansion due to the replacement of sulfur by selenium, leading to a compaction of the film and thereby causing the nanoparticles to merge. During the selenization process, a recrystallization process initiates on the surface of the film, where the interfacial energy is the greatest and the thermal activation barrier of recrystallization is the smallest. These recrystallization fronts are able to produce grains one or more microns in diameter, while the simple ripening of nanocrystals that are far from each interface proceeds much slower.[29] The insufficiently selenized bilayer film (Figure 2b) and large CZTSSe grain films (Figure 2c) accompanied by microcrystalline fractures are subsequently formed. The porosity and specific surface area of different crystalline CZTSSe films are listed in Table 1. The pore size and porosity of CZTSSe films with the enhanced crystallization are relatively low and formed in dense structures in accordance with the SEM morphology, which can be inferred that the electrolyte is difficult to leak into the films through the fractures and almost only active at the surface of the films. In this case, the recrystallization process is accompanied by the variation of morphology from the porous nanostructure to the bulk microstructure, leading to an evident decrease of specific surface area, from 6280.36 to 799.39 m^2/m^2. The decrease of grain boundaries will accelerate electron transport in CZTSSe films.[28]

As the crystallization of CZTSSe film gradually enhanced until large grains formed, the porosity and abundant grain boundaries in the film are dramatically reduced.[28] To further investigate the effect of crystallization on the conductivity of CZTSSe film, we directly conducted resistivity tests using the device with a soda lime float glass (SLG)/CZTSSe/Al structure, and the resistivity data are listed in Table 2. The resistivity of the CZTSSe films with different crystallization exhibits an abrupt decrease from 234.1 Ω·cm of the nanoparticle film to 1.6 Ω·cm of the large-grain film. The surface area decreased by 8 times but the conductivity was enhanced in about 2 degrees, indicating that the charge transport in CZTSSe film would be significantly improved by the enhanced crystallization and decreased grain boundaries.[28]

The crystal structures of CZTSSe films with different crystallization were determined by X-ray diffraction (XRD), as shown in Figure 3a. Eliminating the peaks arising from FTO conductive glass, all the diffraction peaks are attributed to the kesterite phase. The crystal structure of nanoparticle film is undistinguishable by the XRD pattern due to their weak and broad diffraction peaks. However, with the enhancement of the crystallization of CZTSSe films, the XRD peaks become sharper and the minor peaks like (101) are observable,[30] indicating that well crystallization films have been obtained. The major XRD diffraction peaks of the bilayer film and the large-grain film at $2\theta = 27.60$, 45.78, and 54.22° are compatible with major peaks (112), (220), and (312), respectively.

Since some secondary phases, such as Cu_xS, ZnS, ZnSe, and Cu_2SnSe_3, have almost the same XRD patterns with CZTSSe, it is insufficient to determine the phase purity of the CZTSSe film from XRD patterns. Raman spectroscopy was further employed for phase analysis, as shown in Figure 3b. For the films of different crystallization, the main peaks are located at 218 and 329 cm^{-1}, which are in good agreement with the literature,[31] indicating the formation of pure kesterite CZTSSe film.

The photocurrent−voltage properties of DSSCs with different crystalline CZTSSe CEs are shown in Figure 4, and the corresponding data are listed in Table 2. It can be seen that all the DSSCs with CZTSSe CEs possess comparable performances to the Pt-coated DSSC, indicating that CZTSSe is an efficient alternative material. Especially, the enhancement of crystallization of CZTSSe films with increasing heating rate contributes an ordinal increase of J_{sc} and cell efficiency, leading to the highest cell efficiency of DSSC with large-grain CE, which is 13% higher than Pt-coated DSSC. Though the J_{sc} of DSSCs with CZTSSe CEs is higher than that of the Pt electrode prepared by the thermal decomposition H_2PtCl_6 solution method, it cannot be higher than that of efficient nanostructured Pt electrodes, which are not current limiting.[4]

The catalytic activities of CZTSSe films with different crystallization have a direct impact on CE performances. It has been found that the large-grain film with the best crystallization contributes the highest J_{sc} and cell efficiency, suggesting a good electrocatalytic activity to reduce oxidized triiodide to iodide.

Table 1. Porosity and Specific Surface Area Parameters of Different Crystalline CZTSSe Films on FTO

sample	BET surface area (m^2/m^2)	pore volume (cm^3/g)	average pore width (nm)	porosity (%)[a]
nanoparticle	6280.36	0.001750	2.77558	0.6675
bilayer	1812.91	0.001104	6.31712	0.4221
large-grain	799.39	0.000341	4.48188	0.1308

[a]Porosity is calcultated from the BJH pore volume according to $P = V_P/[V_P + (1/3.84)]$, where V_P is the specific cumulative pore volume ($cm^3 \cdot g^{-1}$).

Table 2. Photovoltaic Performances and EIS Data of DSSCs with Different Crystalline CZTSSe CEs and Pt CE

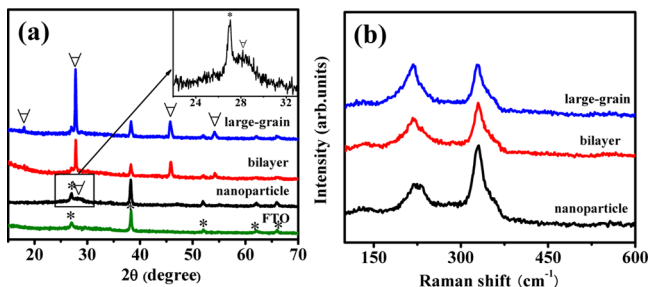| sample	V_{oc} (mV)	J_{sc} (mA/cm^2)	FF (%)	PCE (%)	R_s (Ω)	R_{ct} (Ω)	C_μ (mF)	ρ ($\Omega \cdot$cm)
naonoparticle	694.78	13.46	68.00	6.36	29.64	33.95	0.0653	234.1
bilayer	696.61	14.46	68.10	6.86	35.68	25.97	0.1323	7.088
large-grain	717.73	15.33	67.54	7.43	33.25	9.57	0.1558	1.655
Pt	709.67	12.89	70.91	6.58	28.58	22.8	0.0063	

Figure 3. (a) XRD patterns of different crystalline CZTSSe films and FTO. * and ∀ stand for the XRD peaks of CZTSSe and FTO, respectively. (b) Raman spectra of different crystalline samples.
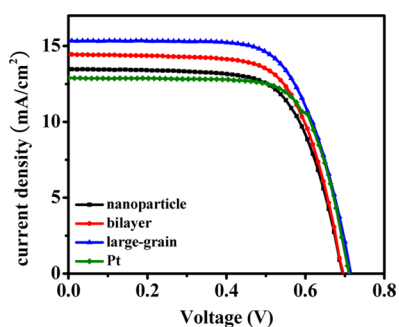

Figure 4. Current density–voltage curves of the DSSCs based on different crystalline CZTSSe CEs and Pt CE, under AM 1.5, 100 mW/cm^2.

To characterize the catalytic activities of the as-prepared CZTSSe CEs, CV measurements under the I^-/I_3^- system were conducted (shown in Figure 5). The more negative pair of peaks in the CV curve correspond to the reduction of I_3^- (reaction 1), and the more positive ones represent the oxidation of I_2 (reaction 2).
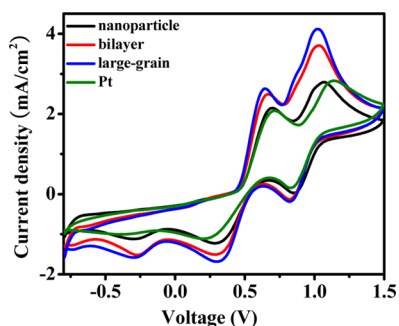
$$I_3^- + 2e^- \rightleftharpoons 3I^- \tag{1}$$

Figure 5. Cyclic voltammograms of CZTSSe CEs with different crystallization and Pt CE. The electrolyte solution was composed of 0.1 M LiClO$_4$, 10 mM LiI, and 1 mM I$_2$ in acetonitrile. The scan rate was 50 mV/s. Pt electrode was used as CE, and Ag/Ag$^+$ works as reference electrode.

$$3I_2 + 2e^- \rightleftharpoons 2I_3^- \tag{2}$$

The CV curves of I^-/I_3^- redox reaction on different crystalline CZTSSe CEs present two pairs of redox peaks and show a more negative pair of peaks than Pt CE, indicating a relatively stronger catalysis of CZTSSe CEs.[32] In addition, the current peak (the left pair of peaks) of CZTSSe CEs is ordinally increased with the enhanced crystallization, demonstrating that the reaction 1 is more efficiently preceded for the well crystalline CZTSSe CE.

EIS is an effective way to reveal the electrochemical characteristics of CE. Herein, EIS of thin-layer symmetrical cells, which were fabricated with two identical electrodes (different crystalline CZTSSe CEs or Pt CEs) adopting the sandwich structure of counter electrodes and electrolyte (CE/electrolyte/CE), is shown in Figure 6. The corresponding
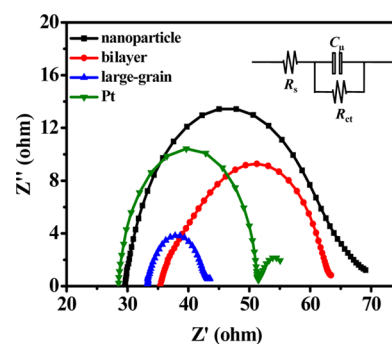

Figure 6. Nyquist plots of CZTSSe CEs with different crystallization and Pt CE. Inset is the equivalent circuit of the symmetric cells.

equivalent circuit is illustrated, where R_{ct} is the charge-transfer resistance at the electrolyte/CE interface, C_μ is the chemical capacitance (corresponding to the accumulated charge density), and R_s is the Ohmic serial resistance, respectively.[15] All of the C_μ, R_s (intercept on the real axis), and R_{ct} (high-frequency hump) values are summarized in Table 2. As seen in the table, the simulated C_μ is slightly increased with the enhanced crystallization from 0.0653 mF (naonoparticle) to 0.1558 mF (large-grain). Though the surface area is abruptly reduced, the R_{ct} is still evidently decreased at a comparable accumulated charge density. Take the bilayer CE and large-grain CE for example, the surface area of large-grain CE is more than 3 times lower than that of bilayer CE, which would induce a larger R_{ct} at a similar charge density and transport process, but the true R_{ct} value is still decreased by more than 2 times. That is to say, the large-grain CE with lower surface area gives a smaller R_{ct} at a similar charge density in comparison to the bilayer CE, due to the improvement of electron transport process. Since the R_{ct} value is corresponding to the catalytic ability of CE,[21] the smallest R_{ct} of the well crystalline CZTSSe CEs at the electrolyte/CE interface finally results in the highest cell efficiency.

Generally, both high surface area and fast charge transport are the key parameters of an ideal CE material. Since the surface area of nanoparticle film is about 8 times larger than that of the large-grain film, we deduce that the smaller resistance of the large-grain film is arising from the decrease of porosity and grain boundaries. Especially, the well crystalline film with the least grain boundaries finally contributes the highest J_{sc} and cell efficiency. We can conclude that the efficient charge transport process will play a dominant role in the reduction of I_3^- if the surface area can meet the requirements of cell performance.

4. CONCLUSIONS

In summary, we employed a convenient solution method and a rapid heating process to prepare well crystalline CZTSSe CEs in DSSCs. The influence of crystallization of CZTSSe film on DSSCs performances was further discussed. It was found that the rapid heating process was beneficial to the formation of well crystalline film with large grains. With the heating rate increased during selenization treatment, the crystallization of CZTSSe film is gradually enhanced and the resistivity of CZTSSe film exhibits an abrupt decrease. Relatively stronger catalysis ability and comparable R_{ct} with Pt are deduced by CV and EIS results. As the highest efficiency of a DSSC with large-grain CEs was achieved, we propose that the efficient electron transport process induced by high crystallization is of great importance to the photovoltaic performances of DSSCs. Further work for efficient DSSCs will be focused on the optimization of material properties, such as the composition and thickness of CZTSSe film, and the crystallization research will make a great contribution in this aspect.

■ AUTHOR INFORMATION

Corresponding Authors
*E-mail: koudongxing@henu.edu.cn (D.K.).
*E-mail: wusixin@henu.edu.cn. Tel/Fax: +860371-23881358 (S.W.).
Notes
The authors declare no competing financial interest.

■ ACKNOWLEDGMENTS

■ REFERENCES

(1) Oregan, B.; Gratzel, M. A Low-Cost, High-Efficiency Solar-Cell Based on Dye-Sensitized Colloidal TiO$_2$ Films. *Nature* **1991**, *353*, 737−740.

(2) Jung, H. G.; Kang, Y. S.; Sun, Y. K. Anatase TiO$_2$ Spheres with High Surface Area and Mesoporous Structure via a Hydrothermal Process for Dye-Sensitized Solar Cells. *Electrochim. Acta* **2010**, *55*, 4637−4641.

(3) Peter, L. M. Dye-Sensitized Nanocrystalline Solar Cells. *Phys. Chem. Chem. Phys.* **2007**, *9*, 2630−2642.

(4) Lin, H.; Hao, F.; Lin, C. F.; Li, J. B. Highly Catalytic Active Nanostructured Pt Electrodes for Dye-Sensitized Solar Cells Prepared by Low Temperature Electrodeposition. *Funct. Mater. Lett.* **2011**, *4*, 7−11.

(5) Yella, A.; Lee, H. W.; Tsao, H. N.; Yi, C. Y.; Chandiran, A. K.; Nazeeruddin, M. K.; Diau, E. W. G.; Yeh, C. Y.; Zakeeruddin, S. M.; Gratzel, M. Porphyrin-Sensitized Solar Cells with Cobalt (II/III)-Based Redox Electrolyte Exceed 12% Efficiency. *Science* **2011**, *334*, 629−634.

(6) Zha, C. Y.; Shen, L. M.; Zhang, X. Y.; Wang, Y. F.; Korgel, B. A.; Gupta, A.; Bao, N. Z. Double-Sided Brush-Shaped TiO2 Nanostructure Assemblies with Highly Ordered Nanowires for Dye-Sensitized Solar Cells. *ACS Appl. Mater. Interfaces* **2014**, *6*, 122−129.

(7) Agarwala, S.; Kevin, M.; Wong, A. S. W.; Peh, C. K. N.; Thavasi, V.; Ho, G. W. Mesophase Ordering of TiO$_2$ Film with High Surface Area and strong Light Harvesting for Dye-Sensitized Solar Cell. *ACS Appl. Mater. Interfaces* **2010**, *2*, 1844−1850.

(8) Agarwala, S.; Peh, C. K. N.; Ho, G. W. Investigation of Ionic Conductivity and Long-Term Stability of a LiI and KI Coupled Diphenylamine Quasi-Solid-State Dye-Sensitized Solar Cell. *ACS Appl. Mater. Interfaces* **2011**, *3*, 2383−2391.

(9) Gong, Y.; Li, C. H.; Huang, X. M.; Luo, Y. H.; Li, D. M.; Meng, Q. B.; Iversen, B. B. Simple Method for Manufacturing Pt Counter Electrodes on Conductive Plastic Substrates for Dye-Sensitized Solar Cells. *ACS Appl. Mater. Interfaces* **2013**, *5*, 795−800.

(10) Huang, X. M.; Qin, D.; Zhang, X. L.; Luo, Y. H.; Huang, S. Q.; Li, D. M.; Meng, Q. B. The Potential of Eutectic Mixtures as Environmentally Friendly, Solvent-Free Electrolytes for Dye-Sensitized Solar Cells. *RSC Adv.* **2013**, *3*, 6922−6929.

(11) Yun, S.; Hagfeldt, A.; Ma, T. L. Pt-Free Counter Electrode for Dye-Sensitized Solar Cells with High Efficiency. *Adv. Mater.* **2014**, *26*, 6210−6237.

(12) Papageorgiou, N.; Maier, W. F.; Grätzel, M. An Iodine/Triiodide Reduction Electrocatalyst for Aqueous and Organic Media. *J. Electrochem. Soc.* **1997**, *144*, 876−884.

(13) Wu, M. X.; Lin, X.; Wang, Y. D.; Wang, L.; Guo, W.; Qu, D. D.; Peng, X. J.; Hagfeldt, A.; Gratzel, M.; Ma, T. L. Economical Pt-Free Catalysts for Counter Electrodes of Dye-Sensitized Solar Cells. *J. Am. Chem. Soc.* **2012**, *134*, 3419−3428.

(14) Cao, Y.; Xiao, Y.; Jung, J. Y.; Um, H. D.; Jee, S. W.; Choi, H. M.; Bang, J. H.; Lee, J. H. Highly Electrocatalytic Cu$_2$ZnSn(S$_{1−x}$Se$_x$)$_4$ Counter Electrodes for Quantum-Dot-Sensitized Solar Cells. *ACS Appl. Mater. Interfaces* **2013**, *5*, 479−484.

(15) Xin, X. K.; He, M.; Han, W.; Jung, J. H.; Lin, Z. Q. Low-Cost Copper Zinc Tin Sulfide Counter Electrodes for High-Efficiency Dye-Sensitized Solar Cells. *Angew. Chem., Int. Ed.* **2011**, *50*, 11739−11742.

(16) Xu, P.; Chen, S. Y.; Huang, B.; Xiang, H. J.; Gong, X. G.; Wei, S. H. Stability and Electronic Structure of Cu$_2$ZnSnS$_4$ Surfaces: First-Principles Study. *Phys. Rev. B* **2013**, *88*, 045427.

(17) Xu, J.; Yang, X.; Yang, Q. D.; Wong, T. L.; Lee, C. S. Cu$_2$ZnSnS$_4$ Hierarchical Microspheres as an Effective Counter Electrode Material for Quantum Dot Sensitized Solar Cells. *J. Phys. Chem. C* **2012**, *116*, 19718−19723.

(18) Dai, P. C.; Zhang, G.; Chen, Y. C.; Jiang, H. C.; Feng, Z. Y.; Lin, Z. J.; Zhan, J. H. Porous Copper Zinc Tin Sulfide Thin Film as Photocathode for Double Junction Photoelectrochemical Solar Cells. *Chem. Commun.* **2012**, *48*, 3006−3008.

(19) Yuan, S. J.; Zhou, Z. J.; Hou, Z. L.; Zhou, W. H.; Yao, R. Y.; Zhao, Y.; Wu, S. X. Enhanced Performance of Dye-Sensitized Solar Cells Using Solution-Based in Situ Synthesis and Fabrication of Cu$_2$ZnSnSe$_4$ Nanocrystal Counter Electrode. *Chem.—Eur. J.* **2013**, *19*, 10107−10110.

(20) Kang, S. H.; Choi, S. H.; Kang, M. S.; Kim, J. Y.; Kim, H. S.; Hyeon, T.; Sung, Y. E. Nanorod-Based Dye-Sensitized Solar Cells with Improved Charge Collection Efficiency. *Adv. Mater.* **2008**, *20*, 54−58.

(21) Li, G. R.; Wang, F.; Jiang, Q. W.; Gao, X. P.; Shen, P. W. Carbon Nanotubes with Titanium Nitride as a Low-Cost Counter-Electrode Material for Dye-Sensitized Solar Cells. *Angew. Chem., Int. Ed.* **2010**, *49*, 3653−3656.

(22) Kim, J.; Kang, J.; Jeong, U.; Kim, H.; Lee, H. Catalytic, Conductive, and Transparent Platinum Nanofiber Webs for FTO-Free Dye-Sensitized Solar Cells. *ACS Appl. Mater. Interfaces* **2013**, *5*, 3176−3181.

(23) Hu, L. H.; Dai, S. Y.; Weng, J.; Xiao, S. F.; Sui, Y. F.; Huang, Y.; Chen, S. H.; Kong, F. T.; Pan, X.; Liang, L. Y.; Wang, K. J. Microstructure Design of Nanoporous TiO₂ Photoelectrodes for Dye-Sensitized Solar Cell Modules. *J. Phys. Chem. B* **2007**, *111*, 358−362.

(24) Jung, Y. K.; Kim, J. I.; Lee, J. K. Thermal Decomposition Mechanism of Single-Molecule Precursors Forming Metal Sulfide Nanoparticles. *J. Am. Chem. Soc.* **2010**, *132*, 178−184.

(25) Alam, N.; Hill, M. S.; Kociok-Koehn, G.; Zeller, M.; Mazhar, M.; Molloy, K. C. Pyridine Adducts of Nickel(II) Xanthates as Single-Source Precursors for the Aerosol-Assisted Chemical Vapor Deposition of Nickel Sulfide. *Chem. Mater.* **2008**, *20*, 6157−6162.

(26) Chesman, A. S. R.; van Embden, J.; Duffy, N. W.; Webster, N. A. S.; Jasieniak, J. J. In Situ Formation of Reactive Sulfide Precursors in the One-Pot, Multigram Synthesis of Cu₂ZnSnS₄ Nanocrystals. *Cryst. Growth Des.* **2013**, *13*, 1712−1720.

(27) Guo, Q. J.; Ford, G. M.; Yang, W. C.; Walker, B. C.; Stach, E. A.; Hillhouse, H. W.; Agrawal, R. Fabrication of 7.2% Efficient CZTSSe Solar Cells Using CZTS Nanocrystals. *J. Am. Chem. Soc.* **2010**, *132*, 17384−17386.

(28) Zhou, H. P.; Hsu, W. C.; Duan, H. S.; Bob, B.; Yang, W. B.; Song, T. B.; Hsu, C. J.; Yang, Y. CZTS Nanocrystals: A Promising Approach for Next Generation Thin Film Photovoltaics. *Energy Environ. Sci.* **2013**, *6*, 2822−2838.

(29) Cao, Y. Y.; Denny, M. S.; Caspar, J. V.; Farneth, W. E.; Guo, Q. J.; Ionkin, A. S.; Johnson, L. K.; Lu, M. J.; Malajovich, I.; Radu, D.; Rosenfeld, H. D.; Choudhury, K. R.; Wu, W. High-Efficiency Solution-Processed Cu₂ZnSn(S,Se)₄ Thin-Film Solar Cells Prepared from Binary and Ternary Nanoparticles. *J. Am. Chem. Soc.* **2012**, *134*, 15644−15647.

(30) Wang, G.; Zhao, W. G.; Cui, Y.; Tian, Q. W.; Gao, S.; Huang, L. J.; Pan, D. C. Fabrication of a Cu₂ZnSn(S,Se)₄ Photovoltaic Device by a Low-Toxicity Ethanol Solution Process. *ACS Appl. Mater. Interfaces* **2013**, *5*, 10042−10047.

(31) Yang, W. B.; Duan, H. S.; Bob, B.; Zhou, H. P.; Lei, B.; Chung, C. H.; Li, S. H.; Hou, W. W.; Yang, Y. Novel Solution Processing of High-Efficiency Earth-Abundant Cu₂ZnSn(S,Se)₄ Solar Cells. *Adv. Mater.* **2012**, *24*, 6323−6329.

(32) He, J.; Lee, L. T. L.; Yang, S. H.; Li, Q.; Xiao, X. D.; Chen, T. Printable Highly Catalytic Pt- and TCO-Free Counter Electrode for Dye-Sensitized Solar Cells. *ACS Appl. Mater. Interfaces* **2014**, *6*, 2224−2228.